

## PROPERTIES OF EXTREMELY RED OBJECTS IN AN OVERDENSE REGION <sup>1</sup>

MARCIN SAWICKI<sup>2,3</sup>, MATTHEW STEVENSON<sup>2,4</sup>, L. FELIPE BARRIENTOS<sup>5</sup>, BRETT GLADMAN<sup>6</sup>, GABRIELA MALLÉN-ORNELAS<sup>7</sup>,  
AND SIDNEY VAN DEN BERGH<sup>2</sup>  
*accepted for publication in ApJ*

### ABSTRACT

We use a serendipitously discovered overdensity of extremely red objects (EROs) to study the morphologies and cumulative surface number density of EROs in a dense environment. Our extremely deep imaging allows us to select very faint EROs, reaching  $K_S=21$ , or  $\sim 2$  magnitudes fainter than the  $L^*$  of passively evolving ellipticals at  $z=1.5$ . We find that the shape of the ERO cumulative surface number density in our overdense field mimics that of the field ERO population over all magnitudes down to  $K_S=21$  but with a factor of 3–4 higher normalization. The excellent seeing in our images ( $0.4''$  in  $K_S$  and  $0.6''$  in  $R$ ) allows for morphological classification of the brighter ( $K_S < 19$ ) EROs and we find a mix of morphologies including interacting systems and disks; the fraction of pure bulges (at most 38%), galaxies with disks (at least 46%), and interacting systems (at least 21%) is consistent with morphological fractions in field ERO studies. The similarity in the shape of the cumulative surface density and morphological mix between our overdense field and the field ERO population suggests that ERO galaxies in overdense regions at  $z \sim 1-2$  may not have had an appreciably different history than those in the field.

*Subject headings:* galaxies: clusters: general — galaxies: evolution — galaxies: high-redshift — galaxies: statistics — infrared: galaxies

### 1. INTRODUCTION

Extragalactic extremely red objects (EROs) are galaxies that have colors consistent with those expected of  $z \gtrsim 1$  passively evolving old stellar populations. As such, EROs are often used to select what are hoped to be direct, passively evolving progenitors of present-day ellipticals in the early universe. However, the extreme red color of EROs (e.g.,  $R-K_S > 5.3$ ,  $R-K_S > 6.0$ ,  $I-K > 4$ , etc.) can also be produced by heavily dust-obscured starbursting galaxies. Despite this possible dichotomy, EROs continue to attract considerable interest since either scenario can represent the direct progenitors of present-day massive galaxies, albeit representing different formation redshifts and histories.

Follow-up studies of ERO samples show that the ERO population is indeed heterogeneous. Spectroscopy reveals that the population is made up of 50–70% absorption-line objects and 30–50% star-forming, emission-line systems (Cimatti et al. 2002; Yan, Thompson, & Soifer 2004a). The distribution of EROs in  $IJK$  or  $RJK$  color-color space also suggests a mix of star-

burst and quiescent systems (e.g., Pozzetti & Mannucci 2000; Smail et al. 2002; Gilbank et al. 2003; Väisänen & Johansson 2004a; but see Moustakas et al. 2004) and Spitzer mid-IR observations show that  $\sim 50\%$  of EROs indeed have high star formation rates ( $\gtrsim 12 M_\odot/\text{yr}$ , Yan et al. 2004b; see also Smail et al. 2002 for VLA results). X-ray observations suggest that a small fraction (5–10%) of EROs host active galactic nuclei (e.g., Roche, Dunlop, & Almaini 2003). Imaging studies of EROs show a variety of morphologies, including bulge-dominated objects, disk galaxies, and interacting systems (Smith et al. 2002; Roche et al. 2002; Yan & Thompson 2003; Gilbank et al. 2003; Moustakas et al. 2004). The strong clustering of EROs (Daddi et al. 2000a, McCarthy et al. 2001) suggests that at least part of the population is associated with massive dark matter halos, and indeed absorption-line EROs are strongly clustered (suggesting they are passively evolving ellipticals) while emission-line ones cluster more weakly (Daddi et al. 2002). The picture of the ERO population is then one of a heterogeneous mix consisting of both quiescent and star-forming objects, some (but not necessarily all) of which may be the direct progenitors of present-day massive elliptical galaxies.

EROs are a strongly clustered population and several very significant ERO overdensities (possibly galaxy proto-clusters?) have been reported in the literature (e.g., Hall & Green 1998; Cimatti et al. 2000; Thompson, Afreth, & Soifer 2000; Best et al. 2003; Toft et al. 2003; Wold et al. 2003; Väisänen & Johansson 2004b). All of these overdensities have been found in dedicated searches that targeted fields of high- $z$  AGN or IR-bright galaxies. These searches focused on confirming that high- $z$  AGN or IR galaxies are good markers of large scale structures at high redshift and/or on studying the spatial distribution of galaxies within them; very little work has been done on systematically comparing ERO properties in overdense

<sup>1</sup> Based on observations collected with the Very Large Telescope at the European Southern Observatory, Chile, as part of ESO programs 65.H-0543(A), 65.S-0513(A) and 69.A-0414(A).

<sup>2</sup> Dominion Astrophysical Observatory, Herzberg Institute of Astrophysics, National Research Council, 5071 West Saanich Road, Victoria, B.C., V9E 2E7, Canada

<sup>3</sup> Present address: Department of Physics, University of California, Santa Barbara, CA 93106, USA

<sup>4</sup> Department of Physics and Astronomy, University of Victoria, P.O. Box 3055, Victoria, B.C. V8W 3P6, Canada

<sup>5</sup> Departamento de Astronomía y Astrofísica, Facultad de Física, Pontificia Universidad Católica de Chile, Casilla 306, Santiago, Chile

<sup>6</sup> Department of Physics and Astronomy, University of British Columbia, 6224 Agricultural Road, Vancouver, B.C., V6T 1Z1, Canada

<sup>7</sup> Harvard-Smithsonian Center for Astrophysics, Mail Stop 15, 60 Garden Street, Cambridge, MA 02138, USA

regions with those of field EROs. However, much can potentially be learned from differences in galaxy properties as a function of environment. In the hierarchical galaxy formation paradigm, galaxies are expected to have started forming first in overdense regions and so EROs in overdensities may represent an older population than those in the field. At the same time, dense environments are thought to affect galaxy *evolutionary* processes through mechanisms such as gas stripping or mergers, resulting in different evolutionary histories in field and cluster galaxy populations. In either case, comparisons between field EROs and EROs in overdense regions may teach us important lessons about the process of galaxy formation in the early universe.

In the present paper we present the results of a very deep study of EROs in a serendipitously discovered overdense region. The original goal of our project was to constrain the surface number density of very faint EROs by exploiting an existing extremely deep ( $R_{lim}>27$ )  $R$ -band image. However, in the course of our analysis we have discovered that we have chanced upon a strong but rare ERO overdensity (see § 4.1) and so have decided to use our extremely deep and high-quality imaging to search for environment-dependent differences in EROs.

Throughout this paper we assume  $\Omega_M=0.3$ ,  $\Omega_\Lambda=0.7$ ,  $H_0=70 \text{ km s}^{-1} \text{ Mpc}^{-1}$ . For consistency with other ERO work, all magnitudes in this paper use the Vega normalization. There are several different definitions of the ERO color selection cut in the literature (e.g.,  $R-K>5.0$ ,  $R-K>5.3$ ,  $R-K>6.0$ ,  $I-K>4.0$ ) that result in different redshift cuts and/or select for different star formation histories. As Yan & Thompson (2003) point out,  $I-K$  selection likely favors systems with more prolonged star formation than do  $R-K$ -selected surveys, and the redder cuts can be expected to be more dominated by dust-enshrouded systems than the bluer cuts. In this paper we use the following two ERO definitions:  $R-K_S > 5.3$  and  $R-K_S > 6.0$ .

## 2. OBSERVATIONS AND DATA PROCESSING

### 2.1. Field Selection

Because of the extreme color of extremely red objects ( $R-K_S > 5.3$  or even  $R-K_S > 6.0$ ), ERO selection requires especially deep  $R$ -band data and only relatively shallow infrared observations. To study *very faint* EROs — to  $K_{lim}\sim 21$  — we need extremely deep  $R$ -band data reaching  $R\sim 27$  over a field large enough to contain a reasonably large number of these fairly rare objects. The acquisition of optical data to such depths is very costly even with 8-meter class telescopes, and so we decided to take advantage of existing ultra-deep  $R$ -band imaging that had already been obtained for another project. Specifically, we used very deep VLT observations of a single pointing that were originally taken to study Solar System objects (Gladman et al. 2001) and that add up to 12 hours of integration on 8.2-meter telescopes. The availability of these extremely deep optical data meant that we could be very economical by only needing to acquire complementary infrared observations.

Our field, centered on R.A.=19:24:11, Decl.=−20:58:40 (J2000.0), is located in the Ecliptic and close to the Galactic plane with Galactic coordinates  $l=17:20:06$ ,  $b=-16:21:18$ . This location presents two potential problems: that of foreground

extinction and that of the presence of a large number of Galactic stars. We address these two problems as follows.

Foreground extinction has the effect of dimming the fluxes and reddening the colors of extragalactic objects. However, the amount of extinction in our field, as measured from the Schlegel, Finkbeiner, & Davis (1998) dust maps, is small —  $A_R=0.23$  and  $A_K=0.03$  — with no evidence for significant variations in the vicinity of our field. Similarly small extinction values are found in the Burstein & Heiles (1982) reddening maps. This amount of extinction does not strongly affect the depth of our data and we explicitly correct for its effects by adjusting our photometric zeropoints in §§ 2.2 and 2.3.

Very bright Galactic stars reduce slightly the effective area of our survey because faint objects are more difficult to detect in the wings of bright stars' light profiles and in the columns of saturated pixels caused by spilled excess charge from saturated stars. Additionally, faint extremely red galactic stars provide a potential source of contamination to our extragalactic ERO sample. We account for these effects by excluding areas affected by very bright stars from our census (§ 4.1) and by constraining the stellar contamination fraction in our catalog using morphological characteristics (§ 3.2). We note that the presence of several bright stars in our field may eventually prove to be a blessing as it allows the intriguing possibility of future follow-up studies of ERO morphologies with adaptive optics.

### 2.2. $R$ -Band Imaging

The  $R$ -band imaging was obtained on 2000 July 26–28 using the ESO VLT 8.2m Unit Telescopes “Antu” and “Kueyen” as part of a search for faint Solar System objects (Gladman et al. 2001). We used the FORS1 imaging spectrograph on UT1 and its FORS2 sibling on UT2. Both FORS1 and FORS2 are equipped with  $2k\times 2k$  CCDs with 0.2 arcsecond pixels, giving a field of view of  $6.8'\times 6.8'$ .

The FORS1 observations were taken in visitor mode and used the Gunn- $r$  (hereafter,  $r$ ) filter, while the FORS2 observations were taken in service mode and used a wider “Special  $R$ ” filter (hereafter  $R_S$ ). Both of these filters have a more sharply defined bandpass than the standard Bessel  $R$  filter that's commonly used in ERO work (see Fig. 1).

All observations were taken in photometric weather and under conditions of very good seeing. The observations were broken into short exposures, with the counts well within the linear regime of the detector. The  $r$  observations (FORS1 in service mode) were dithered between exposures, but the  $R_S$  observations (FORS2 in visitor mode) were undithered. The total integration times were 35000s in  $r$  and 9500s in  $R_S$ , but the effective depths in the two filters were comparable because the  $R_S$  filter has a wider bandpass than the  $r$  filter.

The individual frames were bias subtracted and flat-fielded using standard IRAF<sup>8</sup> tasks before being coadded into a final  $R_S$  image and a final  $r$  image.

<sup>8</sup> IRAF is distributed by the National Optical Astronomy Observatories, which are operated by the Association of Universities for Research in Astronomy, Inc., under cooperative agreement with the National Science Foundation

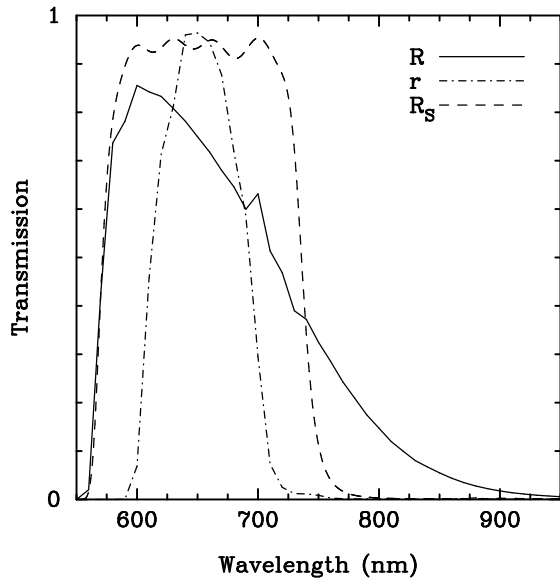


FIG. 1.— Filter transmission curves of the  $R$ ,  $r$ , and  $R_S$  filters. Our observations were taken in  $r$  and  $R_S$ , which have more tightly defined bandpasses than the standard Bessel  $R$  that is generally used in ERO work.

The two images were then flux-calibrated as follows. A first-order flux calibration was applied to each of the two images based on observations of standard stars. Next, the zeropoints were adjusted to correct for foreground Galactic extinction as measured in the Schlegel, Finkbeiner, & Davis (1998) dust map ( $A_R=0.23$ , as mentioned in § 2.1). Finally, the zeropoints were further adjusted to compensate for the differences between our  $R_S$  and  $r$  filters and the  $R$  filter commonly used in ERO work. The necessary adjustment was found by comparing model  $R_S-K_S$ ,  $r-K_S$ , and  $R-K_S$  colors for several plausible ERO spectral energy distributions (SEDs) as shown in Fig. 2. We found that — for EROs — the  $R_S$  zeropoint needed to be decreased by 0.35 mag and the  $r$  one increased by 0.3 mag to bring them into agreement with the  $R$ -band scale. We stress that this is a small *relative* adjustment that transforms well the colors of extremely red objects (but not necessarily those of normal, bluer galaxies) in our  $r$  and  $R_S$  images to the  $R-K_S$  scale commonly used in ERO work.

After the adjustment of the zeropoints of the two master images, the two images were inverse-variance weighted and combined. The edges of the resulting final image — where the S/N was lower because of dithering — were then trimmed, giving a final area of 37.9 arcmin<sup>2</sup> with a total integration time of 44500 seconds. The seeing in the final image, measured on unsaturated stars, was 0.6".

### 2.3. $K_S$ -Band Imaging

The  $K_S$  data were obtained in service mode using ISAAC on the 8.2m VLT Unit Telescope 1 “Antu” during five nights between April 1, 2002 and May 8, 2002. ISAAC’s short-wavelength (1–2.5 $\mu$ m) camera is equipped with a 1k $\times$ 1k Hg:Cd:Te array with 0.148 arcsecond pixels, yielding an instantaneous field of view of 2.5'  $\times$  2.5'. We covered the significantly larger  $R$ -band image by dividing it into four quadrants for infrared imaging. In each

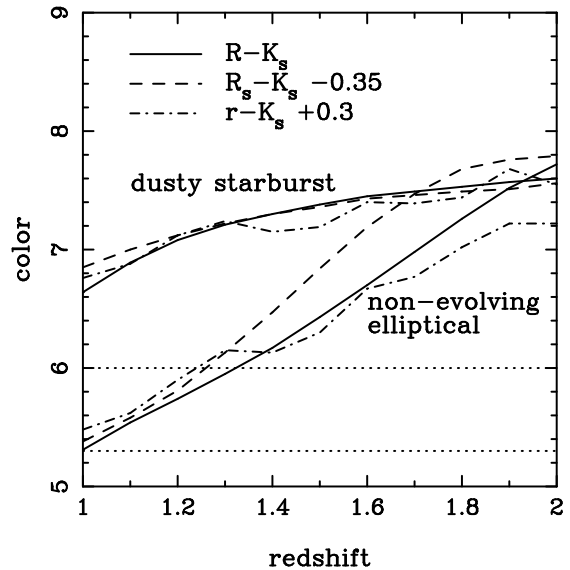


FIG. 2.— Model colors of extremely red galaxies as a function of redshift. The  $R-K_S$  ERO selection thresholds of 6.0 and 5.3 are shown as dotted horizontal lines. The solid, dashed, and dash-dotted lines show the expected colors of dusty starbursts and non-evolving ellipticals in three different photometric systems ( $R-K_S$ ,  $R_S-K_S$ ,  $r-K_S$ ). To compute these colors, we took the 50 Myr-old instantaneous burst from the Bruzual & Charlot (1993) spectral synthesis models substantially reddened with the Calzetti (1997) dust law as well as the elliptical spectral energy distribution from Coleman, Wu, & Weedman (1980), and integrated both these SEDs through the redshifted  $R$ ,  $R_S$ ,  $r$ , and  $K_S$  filter transmission curves. The  $R_S-K_S$  and  $r-K_S$  tracks have been adjusted (by  $-0.35$  and  $+0.3$ , as indicated in the figure) to bring them into agreement with the  $R-K_S$  models.

quadrant we obtained 43 dithered  $K_S$  exposures, each consisting of the average of six 12s integrations, giving us a total integration time of 3096s.

The individual exposures were flat-fielded, sky subtracted, and coadded using the IRAF package DIMSUM. Because DIMSUM did not perfectly correct for the ISAAC bias (a known feature), the bias residuals were subtracted in a separate, final step. This residual removal was done by simply calculating the median value for each row of pixels and then subtracting the median from its respective row, as suggested in the ISAAC Data Reduction Guide (Amico et al. 2002).

The photometric zeropoints were calculated separately for each night using standard star images, and were corrected for foreground Galactic extinction of  $A_K=0.03$  as measured from the Schlegel, Finkbeiner, & Davis (1998) dust maps. The individual images were then stacked together into four master images, one for each quadrant. Three of the four stacked quadrant images comprised the full exposure depth of 3096s. Unfortunately, 22 of the 43 exposures in the north-eastern quadrant had been taken on a night of particularly bad seeing and we decided to exclude them from the final stacking, yielding a final exposure time in that quadrant (only) of 1512s.

Finally, the four stacked quadrant images were astrometrically matched to the  $R$  band image and were combined into a single  $K_S$ -band image of the field. This final  $K_S$ -band image has a FWHM seeing of 0.4", with virtually no variation from quadrant to quadrant.

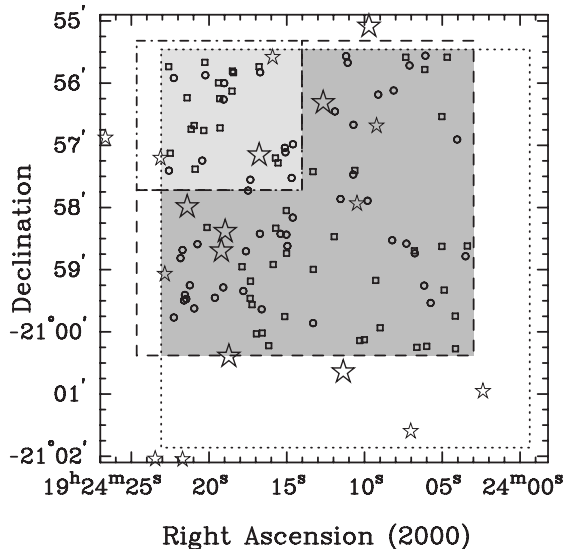


FIG. 3.— Field geometry and the positions of EROs within the field. The dotted line illustrates the area covered by our combined  $R$  image, the dashed line shows the region of 3100s  $K_S$  imaging, with the dot-dashed line box in the north-east corner showing the shallower region of 1500s  $K_S$  exposure. The shaded area shows the area of our final, combined and trimmed images: darker shading indicates the area that received the full 3100s  $K_S$  exposure and lighter shading shows the region that contains only 1500s of  $K_S$  data. Morphologically resolved EROs are shown as squares while morphologically uncertain EROs are marked as circles. Positions of bright stars from the USNO catalog are marked with star symbols: the larger symbols show stars brighter than  $R=14$  and the smaller ones denote stars with  $14 < R \leq 16$ .

#### 2.4. The Final Images

The  $R$  and  $K_S$  images were trimmed to cover the region of mutual overlap and a mask of bad pixels (introduced by the undithered  $R_S$  data) and areas around bright foreground stars was created. Figure 3 shows the geometry of the final images. The size of the final image is  $4.7' \times 4.9'$ , which at  $z=1.5$  corresponds to  $2.4 \text{ Mpc} \times 2.5 \text{ Mpc}$  in the  $\Omega_M=0.3$ ,  $\Omega_\Lambda = 0.7$ ,  $H_0=70 \text{ km s}^{-1} \text{ Mpc}^{-1}$  cosmology. The final good area — the area of the trimmed images that does not contain bright foreground stars or bad pixels — is  $19.6 \text{ arcmin}^2$ , of which  $15.9 \text{ arcmin}^2$  had been imaged to the full 3096s depth in  $K_S$ -band, and the remaining  $3.7 \text{ arcmin}^2$  had the shallower exposure time of 1512s. As determined from simulations (see § 3.3), the limiting magnitude of the  $K_S$  image is  $K_{S,lim}=21.0$  except for the shallower north-east corner, which reaches  $K_{S,lim}=20.6$ .

### 3. THE ERO CATALOG

#### 3.1. Source Detection and Photometry

We used the SExtractor package (Bertin & Arnouts 1996) for object detection and photometry. Object detection was done on the  $K_S$ -band image, and we required 5 contiguous pixels to be above the threshold of  $2.2\sigma_{sky}$  for a candidate to be considered an object.  $K_S$ -band magnitudes were measured within SExtractor’s “best” apertures, which are Kron-like apertures for the majority of objects except for objects suspected of having close companions, for which isophotal magnitudes are used instead (Kron 1980; Bertin & Arnouts 1996).  $R-K_S$  colors were measured in matched  $1.0''$ -diameter apertures on

the  $R$ -band image and on a copy of the  $K_S$ -band image that had been Gaussian-smoothed to match the poorer,  $0.6''$  seeing of the  $R$ -band data. We checked the  $K_S$ -band number counts of objects classified as resolved by SExtractor and found that they are in good agreement with galaxy counts in the literature (e.g., Bershady, Lowenthal, & Koo 1998; Totani et al. 2001).

#### 3.2. Star-Galaxy Classification

L- and M-type dwarfs are sufficiently red to be included in our ERO color cut and so at the low Galactic latitude of our field our ERO sample may be contaminated by a significant number of Galactic stars. We used the morphological appearance of our objects in the  $0.4''$   $K_S$ -band image to constrain the amount of such foreground stellar contamination. We classified the morphologies of our EROs both by using automated neural-network classification in SExtractor and by visual inspection by two of the authors (MS and MS). The human classifiers categorized objects as either “resolved” or “uncertain”, where “resolved” were those EROs which had clearly extended morphologies that made them extremely unlikely to be foreground stars. The automated classification by SExtractor yielded results consistent with the human classification. We present results of the human star/galaxy ERO classification in the rest of this paper, although we note that the results do not differ significantly if we use the SExtractor neural network results. Column 6 in Table 1 lists the results of our Resolved/Uncertain classification.

Throughout the rest of the paper our approach is to assume that EROs classified as “R” (Resolved galaxies) are indeed high- $z$  galaxies, whereas objects classified as “U” (Uncertain) may contain a mixture of more compact galaxies and foreground stars. The R subsample thus gives a robust and very conservative *lower limit* on extragalactic ERO number density, while the entire R+U sample gives a conservative upper limit.

The “R” sample thus contains extragalactic EROs only, with no stellar contamination. However, the “U” sample should contain very few stellar contaminants for the following reason. At brighter magnitudes ( $15 < K_S < 19$ ), our ERO catalog contains only 3/24 (13%) potential stars (see also Fig. 6). Since the ratio of stars to galaxies generally decreases towards fainter magnitudes, the stellar fraction is likely to be even lower at  $K_S > 19$  than it is at  $K_S < 19$ . Most of the faint “U” objects are thus likely to be classified as such not because they are stars but because they have low S/N that prevents us from seeing extended structure. Thus, while the U sample gives a very hard lower limit, we can reasonably assume that the true counts of extragalactic EROs are very close to those given by the combined R+U sample.

#### 3.3. Completeness

We used simulations to test the accuracy of our photometry and to understand and correct for the incompleteness of our survey. Specifically, we inserted artificial objects of known flux and color at random positions in our images and then repeated the object-finding and photometry procedures of § 3.1 to determine the completeness of our catalog and its photometric accuracy by measuring the recovered fraction, magnitudes, and colors of the artificial objects. We surveyed the parameter

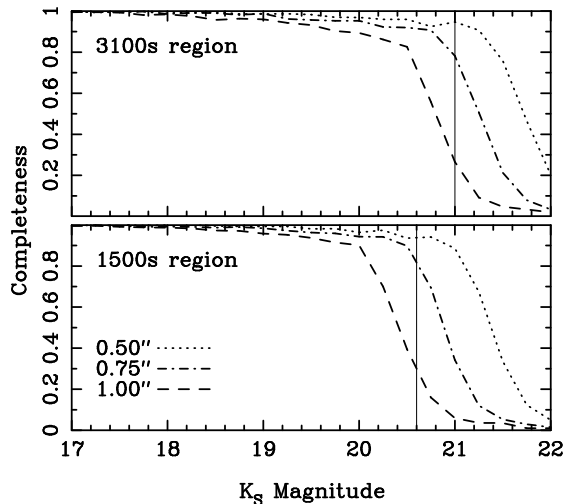


FIG. 4.— Detection completeness in the  $K_S$  image derived using simulations described in § 3.3. The top panel illustrates the completeness in the 3100s integration region, while the lower panel shows the completeness in the 1500s quadrant. The three different curves are for objects with FWHM of  $0.50''$ ,  $0.75''$ , and  $1.00''$ . The  $0.75''$  curve was used to correct for incompleteness of the ERO surface number density. (§ 4.1). The vertical lines indicate our adopted 80% completeness limits.

space spanning a range of magnitudes ( $17 \leq K_S \leq 22$ ) and colors ( $4 \leq R - K_S \leq 8$ ) with a sufficiently large number of realizations (1000 artificial objects at each seeing, color, and magnitude step) so as not to be dominated by small number statistics. We conducted these tests using artificial objects with Gaussian profiles of  $0.5''$ ,  $0.75''$ , and  $1.0''$  FWHM.

Figure 4 shows the completeness functions determined from our simulations. As expected, completeness is higher at a given magnitude in the deeper, 3100s portion of the image than in the shallower, 1600s quadrant. Also, not surprisingly, completeness depends on the size of the object. Because the typical sizes of objects in our ERO catalog (§ 3.1) were  $\text{FWHM} \leq 0.75''$ , we decided to adopt the curves for  $0.75''$  as a conservative incompleteness estimate. In the deeper, 3100s portion of the image, the 80% completeness is reached at  $K_{S,lim} \sim 21$ , and in the shallower, 1600s quadrant, it is reached at  $K_{S,lim} \sim 20.6$ . We note that these limiting magnitudes are, at 80%, conservative. We could have defined fainter limits by choosing 50% or even 20% completeness but we chose 80% completeness to ensure results that are conservatively robust.

Our simulations also showed that there were no significant biases in the measurement of colors of EROs down to our adopted completeness limit, and that the brightness and color error estimates given by SExtractor were accurate for our purposes.

#### 3.4. The ERO Catalog

EROs were identified solely on the basis of their  $R - K_S$  colors. Figure 5 shows the color-magnitude diagram of all the red objects in our field and Table 1 presents the positions,  $K_S$  magnitudes, and  $R - K_S$  colors of all EROs. For the purposes of our catalog, EROs are defined to be all objects that are above our adopted completeness limits and are redder than  $R - K_S = 5.3$ . They are plotted with large symbols in Fig. 5: filled squares denote

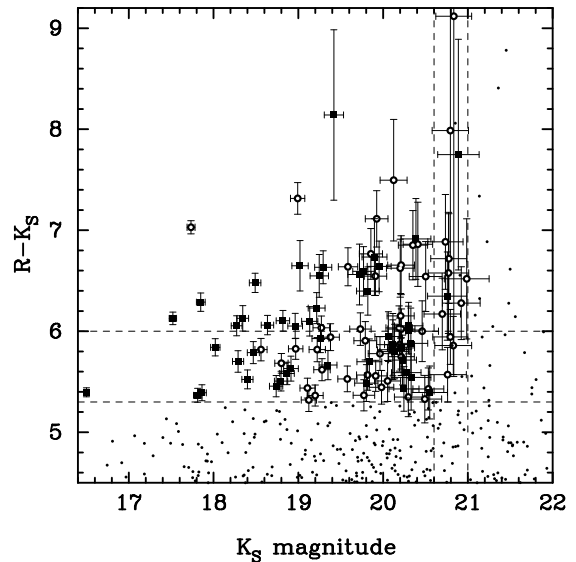


FIG. 5.— Color-magnitude diagram of red objects in our field. Filled squares show objects morphologically classified as resolved galaxies and open circles denote morphologically uncertain objects. Non-EROs and objects fainter than the completeness limit are plotted as dots. The vertical dashed lines denote our completeness limits and the horizontal ones indicate the ERO color selection cuts. Error bars show  $1\sigma$  uncertainties measured by SExtractor.

objects that are morphologically resolved and therefore very likely distant galaxies, while open circles show objects with uncertain morphologies. In total, to  $K_S = 21.0$ , our catalog contains 101  $R - K_S > 5.3$  of which 49 are also  $R - K_S > 6.0$  EROs. It is worth pointing out that our  $R$ -band data are deep enough that all  $K_S$ -selected objects are also detected in  $R$ .

## 4. ANALYSIS

### 4.1. Surface Number Density

Figure 6 shows the cumulative ERO surface number density in our field for both  $R - K_S > 5.3$  and  $R - K_S > 6.0$  EROs. These measurements have been corrected for incompleteness, although — as Fig. 4 shows — the correction is small even at the limit of our catalog. Our surface number densities are shown both for morphologically resolved EROs (upward-pointing triangles) and for all EROs, including resolved and unresolved ones (downward-pointing filled triangles). As we pointed out in § 3.2, these two categories of EROs represent the extremes of the plausible extragalactic ERO surface number density in our field in that the former class is virtually guaranteed to be free of stellar contamination thus giving a robust lower limit, whereas the latter includes all possible extragalactic EROs — including compact galaxies — and so gives an upper limit. The true extragalactic ERO surface number density thus lies somewhere between the bounds defined by the upward- and downward-pointing filled triangles, although we expect their true surface number density to be far closer to the upper limit as explained in § 3.2.

The most striking feature of Fig. 6 is that the ERO surface number density in our field is  $\sim 3$ – $4$  higher than that seen in other surveys (e.g., Thompson et al. 1999; Daddi et al. 2000b; Smith et al. 2002). This is true for both the  $R - K_S > 5.3$  and  $R - K_S > 6.0$  EROs, and holds at all

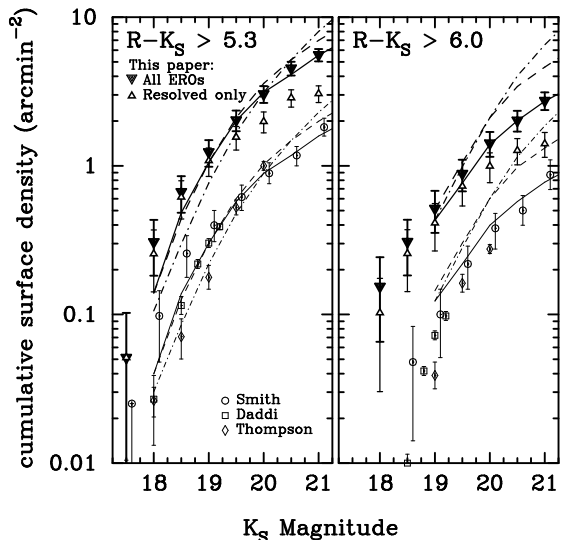


FIG. 6.— Cumulative surface number density of EROs for both color selection cuts. Triangles show our counts, for *all* EROs (downward pointing filled triangles) and for only those thus bracket the actual surface number density of extremely red galaxies in our field, although the true ERO counts are likely to be close to the full counts (filled, downward pointing triangles), as we argue in § 3.2. The data have been corrected for incompleteness, although this correction is small. Open symbols show measurements from field ERO surveys (Thompson et al. 1999; Daddi et al. 2000b; Smith et al. 2002). The *thin* solid, dashed, and dot-dashed curves are Daddi et al. (2000b) PLE models with  $\tau = 0.1$  Gyr and  $z_f = 2.5, 3.0,$  and  $10.0$  (see Smith et al. 2002); their vertical scaling is dictated by the observed luminosity function of ellipticals in the local universe. The upper, *thick* curves are the very same PLE models simply shifted upwards in surface number density by a factor of 3.5.

but the faintest magnitudes,  $K_S \sim 21$ , where the number of objects for which we are unable to make a star/galaxy determination becomes large. Even at this faint end, however, our field is overdense in resolved EROs compared to other surveys, and it is very likely that the overdensity remains as high as a factor of  $\sim 3$ – $4$  at all magnitudes  $K_S \leq 21$  given the upper limits on the ERO surface number density and the fact that — as we discussed in § 3.2 — the true counts are actually likely to be close to this upper limit.

Finally, we note the significant gradient in the surface number density of EROs in our field. As Fig. 3 shows, the ERO density increases from west to east, with the eastern half of the field containing nearly twice as many EROs (65) as the western half (36). The excess in the eastern half may in fact be even higher than that given that the north-eastern quadrant of our catalog has a shallower completeness limit than the rest of the field. In any case, the gradient is highly significant, since a 65:36 or 36:65 ratio occurs only  $\sim 0.5\%$  of the time in a random distribution. The number density gradient raises in the direction of the 4 mJy 1.4GHz radio source NVSS J192430-205733 (Condon et al. 1998), which is located only  $\sim 2'$  from the eastern edge of our field (if we assume that the 65:36 gradient has to rise *towards* the radio source, then the probability of the gradient being a random artefact is even lower, namely  $\sim 0.25\%$ ). While no redshift or photometry at other wavelength is available for this source, it is not implausible that the source may reside in the

ERO structure with the ERO density gradient pointing towards it.

#### 4.2. A cluster of EROs?

The most plausible explanation of this ERO overabundance is that we have discovered a true physical overdensity of EROs. The existence of an ERO overdensity is not surprising given that EROs are known to be strongly clustered (e.g., Daddi et al. 2000a; Roche et al. 2002), although a factor of 3–4 excess is very rare in a random field the size of ours: Daddi et al. (2000a) show that a  $>3$ -fold excess would occur in fewer than 0.1% randomly placed 25 arcmin<sup>2</sup> fields even for luminous ( $K_S \leq 18.8$ ), possibly *more* clustered, EROs. However, ERO overdensities as rich as the one reported here have been discovered by surveys that target the fields of high- $z$  AGN (e.g., Hall & Green 1998; Cimatti et al. 2000; Hall et al. 2001; Wold et al. 2003), and mid-IR bright galaxies (Väisänen & Johansson, 2004b). For example, Wold et al. (2003) find that to their  $K_S \sim 19$  limit, the average number density of EROs in their 13 QSO fields is a factor of 2–3 higher than that in random-field surveys, and Väisänen & Johansson (2004b) find an excess of 2–5 in a number of small fields centered on ISO mid-IR selected objects. At any rate, our 3–4-fold density excess is entirely consistent with the results of such surveys that target fields around known high- $z$  objects, although our imaging traces the excess to a significantly fainter level ( $K_S = 21.0$ ), or  $\sim 2$  magnitudes below  $L^*$  at  $z \sim 1.5$ .

Our 3–4-fold surface overdensity may imply a much higher *physical* overdensity. Whereas the field ERO population is distributed over a likely redshift range  $z \sim 1$ – $2$ , our excess EROs may well be located in a protocluster or a filament, spanning a volume that corresponds to a much smaller  $\Delta z$ . We have no way of knowing what that volume is with just the data in hand, but we can make a very rough, illustrative estimate of the physical overdensity as follows. If we assume that the field ERO population uniformly spans  $z = 1$ – $2$  but that the EROs in our overdensity reside in a cube with line-of-sight depth equal to the angular size of our field (i.e.,  $\sim 2.5$  Mpc  $\times$   $2.5$  Mpc  $\times$   $2.5$  Mpc, comoving units), then — after statistically correcting for foreground/background ERO contamination based on field ERO counts — the spatial density of EROs in the structure is  $\sim 5000$  higher than that of the field ERO population. The factor of  $\sim 5000$  is a rough *upper limit* on the overabundance of EROs in the structure. If, for example, we assume that the line-of-sight extent of the structure is 25 Mpc instead of 2.5 Mpc then the spatial density in the structure is reduced to  $\sim 500$  times that of the field population. Similarly, if the redshift depth occupied by the *field* ERO population is smaller than the  $\Delta z = 1$  we assumed here, then the overdensity factor will also be reduced. In any case, however, as long as the overdensity we have discovered is physical then the relatively small 3–4-fold number excess translates into a substantial spatial overdensity that may rival that of rich clusters in the present-day universe.

Finally, we note that it is possible that the radio source NVSS J192430-205733 located just off the eastern edge of our field may be a high- $z$  object that is part of the same structure as the EROs. This possibility is supported by the ERO density which increases in the direction of the radio source. However, at present no redshift (or any

other) information is available on this object and confirmation of this hypothesis will need further observations.

#### 4.3. Comparing ERO populations in the overdensity and in the field

The depth of our data and the excellent seeing in our images allows us to study the properties of the ERO population in our overdense region. Differences between the ERO population in this overdensity and in the field may give interesting clues to the nature of EROs, to the origin and evolution of present-day early-type galaxies, and to the populating of large galaxy structures in the early Universe. We focus here on comparing the surface number density to  $K_S=21$  and on morphologies of brighter,  $K_S<19$ , EROs.

##### Surface number density

The ERO surface number density in our overdense field is higher than in field ERO surveys at *all* magnitudes down to  $K=21$ . If — as we have argued in § 3.2 is likely the case — our true ERO surface number density is close to our upper limits (downward-pointing filled triangles) in Fig. 6, then the difference between our ERO overdensity and EROs in the general field is consistent with a straightforward overall 3–4-fold increase in number density, *irrespective of magnitude*. This similarity extends so far as to the presence of a break in the slope of field ERO surface number density at  $K_S\sim 19$ –20 (Smith et al 2002; Roche, Dunlop & Almaini 2003). We conclude that the surface number density in our ERO overdensity is consistent with a straightforward increase in number density of EROs, irrespective of ERO brightness.

The fact that the surface number density slope does not vary with environment is surprising: we might have expected to see environmental variations given that the “galaxy formation clock” is expected to turn on earlier in overdense regions and that environment can modify subsequent galaxy evolution in high-density regions through processes such as tidal stripping, ram-pressure stripping, suppression of galaxy-galaxy mergers, and the aging of stellar populations.

Daddi et al. (2002b), among others, have generated ERO surface number density predictions using pure luminosity evolution (PLE) models which attempt to model EROs as elliptical galaxies by assuming that they form all of their stars at some high redshift,  $z_f$ , that these stellar populations evolve passively ever since, and that at the epoch we observe them they are already located in galaxies that follow a luminosity function that by  $z=0$  will fade to be consistent with that of present-day ellipticals. These PLE models can reproduce reasonably well the field ERO surface number density, as is illustrated by the thin curves in Fig. 6 (Smith et al. 2002). The faint-end slope of these models compared with the field ERO surface number density suggests a redshift of formation of  $z_f\sim 2.5$  for the field  $R-K_S > 6.0$  EROs (the case for  $R-K_S > 5.3$  EROs is less unambiguous but also consistent with this moderate formation redshift).

Adjusting the Daddi et al. PLE models upwards in density by a factor of 3.5 brings them into agreement with the surface number density of *bright* EROs (both  $R-K_S > 5.3$  and  $R-K_S > 6.0$ ) in our field (see Fig. 6). The  $z_f=2.5$  models are then in good agreement with our ERO counts both for  $R-K_S > 5.3$  and  $R-K_S > 6.0$

EROs down to our limit of  $K_S=21$ . This is again unexpected because we would have expected galaxy formation to begin earlier in our overdense region than in the field, with  $z_f>2.5$  and hence a steeper faint-end slope of the  $R-K_S > 6.0$  counts. However, the models with higher formation redshifts —  $z_f=10$  and even  $z_f=3$  — are steeper than the observed counts at the faint end.

The fact that the same  $z_f=2.5$  model (modulo a density normalization) fits best both the field ERO population *and* the ERO population in our overdensity suggests that field and cluster EROs may share the same evolutionary history regardless of their present environment. Since neither population is well fit by the  $z_f=3$  model further suggests that the field and cluster ERO populations may in fact be co-eval or nearly co-eval. We note that this argument is not strongly sensitive to the details of the models: since we are comparing two identically-selected populations that are best fit by the same model, any systematic change in the model that may affect the model’s details (such as the  $z_f$ ) will apply equally to the field and cluster population. Consequently, the conclusion about the co-evalness of the cluster and field populations is fairly robust under the assumption that the two populations are composed of similar objects. This conclusion can, however, be affected if the two populations are composed of distinct subpopulations (e.g., a mix of old, quiescent galaxies and dusty starbursts) that are present in proportions that vary between the field and the cluster, but that conspire to reproduce the observed magnitude dependence of the cumulative surface number density. We constrain this possibility of a different mix of subpopulations next.

##### Morphologies

At low and intermediate redshifts the morphological mix of galaxies depends on environment, with denser environments being significantly richer in early-type galaxies than the field (e.g., Hubble 1936; Dressler 1980; Hashimoto & Oemler 1999; Goto et al. 2003). If the same environmental trends hold at high redshift, we should expect more passively evolving old stellar populations and fewer dusty starburst EROs in our overdensity than in the field. Given the excellent  $0.4''$  seeing in our  $K_S$  image, we decided to compare the morphologies of the brighter EROs in our sample with those of field ERO morphological studies in the literature. We focus on EROs brighter than  $K_S=19$ , where the S/N in our images is high, and where we have a good chance of detecting fainter companions, disturbed morphologies, or other potential signs of galaxy-galaxy interactions. Postage stamp images of our  $K_S<19$  EROs are shown in Fig. 7.

There are 24 EROs with  $R-K_S > 5.3$  and  $K_S<19$  in our sample and three of us (SvdB, MS, and MS) have visually classified their morphologies in both the  $R$  and  $K_S$  images simultaneously. Table 2 compiles the results of this morphological classification. Of the 24 EROs, eleven show clear evidence for the presence of disks (usually together with bulges), and five objects have signs of ongoing interactions or very close companions.

We next ask whether the morphological mix in our ERO overdensity is different than the mix in the field ERO population. In doing so we will be conservative by counting only those objects with clearly detected disks to give us a lower limit on the disk fraction, and counting *all*

those objects without detected disks or signs of interaction to give us an upper limit on the fraction of passively evolving ellipticals. Using this approach we find that *at least* 11/24 (i.e., >46%) of the EROs in our field have disks and *at least* 5/24 (>21%) are interacting. At most 9/24 (<38%) may be passively evolving ellipticals. The actual fraction of disks may be higher than 46% because faint disks are hard to see against the sky background; at the same time, the actual fraction of passively evolving ellipticals may be lower than 38% because here we have conservatively assumed that the three point-source objects which are unresolved are pure-bulge galaxies rather than foreground stars and that objects that are resolved but for which we were unable to make a morphological decision nevertheless are pure bulge EROs. Our  $R-K_S > 6.0$  sample, although consisting of only ten  $K_S < 19$ , objects contains a similar morphological mix of *at least* 40% (4/10) disks and *at most* 50% (5/10) pure bulges.

Comparing morphological fractions between different surveys is complicated because different surveys use different morphological classification schemes and work with imaging data of different quality. Moreover, different surveys use different color selection systems (e.g.,  $R-K_S$ ,  $I-K$ ) to define EROs, resulting in sensitivity to different star formation histories (see Yan & Thompson 2003 for a discussion) and hence, potentially, to different morphologies. Additionally, even when the same filter system is used, different color cuts within that system (e.g.,  $R-K_S > 5.0$ ,  $R-K_S > 5.3$ ,  $R-K_S > 6.0$ ) select populations spanning different redshift ranges or obscured by different amounts of interstellar dust (see, e.g., Fig. 2). Although all these effects limit the value of comparisons between different surveys, it is nevertheless interesting to compare the morphological mix in our ERO overdensity with that found in field ERO surveys in order to look for gross trends.

The morphological mix of at least 46% disks, less than 38% passively evolving ellipticals, and at least 21% interacting systems in our  $R-K_S > 5.3$ ,  $K_S < 19$  sample is consistent with recent *field* ERO studies. Specifically, our morphological mix is consistent with the HST study of  $R-K_S > 5.3$  EROs in the GOODS-N field by Moustakas et al. (2004) who found 33-44% of their EROs to be early-type; it is also consistent with the HST study by Smith et al. (2002) of  $R-K > 5.3$  EROs who found a 65% fraction of disks and irregulars; with the Yan & Thompson HST study of bright  $I-K > 4$  EROs who found that 30% are bulge-dominated, 65% are disk-dominated, and 17% are mergers or interacting systems; with the Gilbank et al. (2003) study of  $I-K > 4$  EROs who found that 35% have disk components, up to 30% are spheroidal, and 15% are disturbed or irregular; and with the Roche et al. 2002 ground-based study of  $R-K > 5.0$  EROs who found a 3:2 mixture of bulge and disk light profiles with  $\sim 25\%$  showing signs of interaction. All these recent morphological studies of *field* EROs find that the population consists of a mixture of bulge- and disk-dominated systems, with the bulge-dominated systems being in the minority (at  $\sim 1/3$  of the total) and, moreover, contains a small but sizeable fraction of  $\sim 1/5$ - $1/4$  of interacting systems. Our morphological fractions are entirely in line with these field ERO studies, and we conclude that there is no evidence for difference in ERO morphological mix between

the overdense region and the field.

## 5. SUMMARY, DISCUSSION, AND CONCLUSIONS

In this work we used a deep  $K_S$ -band image of a field with existing extremely deep  $R$ -band imaging to study the properties of EROs in an overdense region. These deep images allowed us to robustly select both  $R-K_S > 5.3$  and  $R-K_S > 6.0$  EROs down to  $K_S=21$  (80% completeness) over most of the image. The ERO surface number density in our field is 3-4 times higher than in the literature, which represents a very significant excess even given the strong clustering of EROs. This excess leads us to us to conclude that our field may contain a physical structure of EROs — possibly a filament or a protocluster — which could have a *physical* ERO density of up to  $\sim 5000$  times that of the field ERO population.

We used the excellent depth of our data ( $K_{S,lim}=21$  over most of the field) to examine the shape of the ERO number counts in our field. We found no evidence in the cumulative ERO surface number density that the ERO population in our ERO overdensity is different from that in the field: aside the overall increase in normalization, the surface number density of EROs in our structure is consistent with that of field EROs to within the uncertainties down to at least  $K_S=20.5$  and includes evidence for a break in slope at  $K_S=19-20$ .

We then use the excellent image quality of our data ( $0.4''$  in  $K_S$ ,  $0.6''$  in  $R$ ) to classify the morphologies of bright EROs,  $K_S < 19$ , where we have sufficient S/N to detect faint features above the sky background. We found that the morphological mix of bright EROs in our structure is similar to that found in morphological studies of field EROs. Specifically, we found that of the 24  $K_S < 19$  EROs in our structure, *at least* 11 (46%) have evidence for disks and *at most* nine (38%) can be passively evolving ellipticals. We also find that at least five (21%) show signs of galaxy-galaxy interactions. These morphological mixes are in line with morphological fractions of field EROs, and we concluded that there is no evidence that the cluster and ERO populations differ in their morphological composition.

The consistency of morphological fractions between our sample and field ERO samples and the similarity of the shape of the number counts, both suggest that the ERO population does not vary strongly with environment. This lack of environmental differences between field and overdensity EROs is surprising. The hierarchical structure formation paradigm suggests that galaxy formation begins earlier in overdense regions and consequently we might have expected the ERO population in the overdensity to be more evolved, with more passively evolving ellipticals and fewer star-forming disks than in field ERO samples. Similarly, if the galaxy formation clock has started at an earlier redshift in our ERO structure, we might have expected a steeper faint-end slope of the ERO cumulative surface number density as suggested by some PLE models. At present, however, we are forced to conclude that there is no evidence for environmental dependence of the ERO galaxy population.

One explanation for this surprising similarity between field and overdensity EROs is that the EROs in our overdensity did *not* form in it but formed in the field instead (and thus are coeval with the field ERO population) and fell into the overdensity at a later time. The fact that



the morphological mix is not significantly different from the field population and includes a large proportion of presumably star-forming disks suggests further that the infall was recent or that the overdense environment is not yet efficient at modifying — or has not yet had time to modify — the morphologies of the galaxies it contains through gas stripping and other processes that have been suggested to operate at lower redshifts.

Environmental differences can teach us much about how massive galaxies as traced by EROs form and evolve at high redshift, and we feel that the present work is just the beginning of such studies. Spectroscopic observations of EROs in our overdense field should prove very valuable as they would not only allow us to compare spectral characteristics of our cluster ERO population with field EROs (as studied by, e.g., Cimatti et al. 2002 and Yan et al. 2004a), but would also let us understand the ERO redshift distribution in our field, potentially giving important information about the line-of-sight size of the structure and/or its mass. Spitzer Space Telescope mid-IR observations can be used to constrain the number of actively star-forming galaxies among our cluster EROs, and the comparison of their abundance with that amongst field EROs (Yan et al. 2004b) may teach us about how star formation in EROs depends on their environment. Additionally, since our field contains a relatively large

number of bright stars (see Fig. 3), our morphological study can be improved with adaptive optics imaging. Finally, other known ERO overdensities should be *systematically* studied to assemble a larger set from which to draw more robust conclusions. Several significant ERO overdensities have now been reported in the literature (e.g., Hall & Green 1998; Cimatti et al. 2000; Best et al. 2003; Toft et al. 2003; Wold et al. 2003, Väisänen & Johansson 2004b) and deep optical/NIR imaging, mid-IR photometry, and spectroscopic follow-up will give a valuable data set with which to study environmental differences that impact the formation and evolution of massive galaxies.

We thank the ESO Paranal staff for their work in obtaining these data. We also thank Jerzy Sawicki, David Thompson, Wayne Barkhouse, and the anonymous referee for useful comments and discussions. This work made use of the NASA Extragalactic Database (NED). GMO is supported by a Clay Fellowship at the Smithsonian Astrophysical Observatory. This research was partly financed by the Centro de Astrofísica FONDAF, CONICYT, Chile.

## REFERENCES

- Amico, P., Cuby, J. G., Devillard, N., Jung, Y., & Lidman, C., 2002, ISAAC Data Reduction Guide 1.5, European Southern Observatory
- Bershady, M.A., Lowenthal, J.D., & Koo, D.C. 1998, ApJ505, 50
- Bertin, E. & Arnouts, S. 1996, A&AS, 117, 393
- Best, P.N., Lehnert, M.D., Miley, G.K., & Röttgering, H.J.A. 2003, MNRAS, 343, 1
- Bruzual A., G. & Charlot, S. 1993, ApJ, 403, 538
- Burstein, D. & Heiles, C. 1982, AJ, 87, 1165
- Calzetti, D. 1997, in AIP Conf. Proc. 408, The Ultraviolet Universe at Low and High Redshift, eds. W.H. Waller et al. (New York: AIP), 403
- Cimatti, A., Villani, D., Pozzetti, L., & di Serego Alighieri, S. 2000, MNRAS, 318, 453
- Cimatti, A. et al. 2002, A&A, 381, L68
- Coleman, G.D., Wu, C.-C., & Weedman, D.W. 1980, ApJS, 43, 393
- Condon, J.J., Cotton, W.D., Greisen, E.W., Yin, Q.F., Perley, R.A., Taylor, G.B., & Broderick, J.J. 1998, AJ, 115, 1693
- Daddi, E., Cimatti, A., Pozzetti, L., Hoekstra, H., Röttgering, H. J. A., Renzini, A., Zomorani, G., & Manucci, F. 2000a, A&A, 361, 535
- Daddi, E., Cimatti, A., & Renzini, 2000b A&A, 362, L45
- Daddi, E. et al. 2002, A&A, 384, L1
- Dressler, A. 1980, ApJ, 236, 351
- Gilbank, D.G., Smail, I., Ivison, R.J., & Packham, C. 2003 MNRAS, 346, 1125
- Gladman, B., Kavelaars, J., Petit, J.-M., Morbidelli, A., Holman, M. J., & Lored, T. 2001, AJ, 122, 1051
- Goto, T., Yamaguchi, C., Fujita, Y., Okamura, S., Sekiguchi, M., Bernardi, M., & Gomez, P.L 2003, MNRAS, 346, 601
- Hall, P.B., & Green, R.F. 1998, ApJ, 507, 558
- Hall, P.B., et al. 2001, AJ, 121, 1840
- Hashimoto, Y. & Oemler Jr., A. 1999, ApJ, 510, 609
- Hubble, E. 1936, The Realm of the Nebulae (New Haven: Yale University Press), p. 55
- Kron, R.G. 1980, ApJS, 43, 305
- McCarthy, P.J., et al. 2001, ApJ, 560, L131
- Moustakas, L.A., et al. 2004, ApJ, 600, L131
- Pozzetti, L. & Mannucci, F. 2000, MNRAS, 317, L17
- Roche, N. D., Almaini, O., Dunlop, J., Ivison, R. J., & Willott, C. J. 2002, MNRAS, 337, 1282
- Roche, N.D., Dunlop, J., & Almaini, O. 2003, MNRAS, 346, 803
- Schlegel, D. J., Finkbeiner, D. P., Davis, M. 1998, ApJ, 500, 525
- Smail, I., Owen, F.N., Morrison, G.E., Keel, W.C., Ivison, R.J., & Ledlow, M.J. 2002, ApJ, 581, 844
- Smith, G.P., Smail, I., Kneib, J.-P., Czoske, O., Ebeling, H., Edge, A.C., Pelló, R., Ivison, R.J., Packham, C., & Le Borgne, J.-F. 2002, MNRAS, 330, 1
- Thompson, D., Beckwith, S.V.W., Fockenbrock, R., Fried, J., Hippelein, H., Huang, J.-S., von Kuhlmann, B., Leinert, Ch., Meisenheimer, K., Phleps, S., Röser, H.-J., Thommes, E., & Wolf, C. 1999, ApJ, 523, 100
- Thompson, D., Aftreth, O., & Soifer, B.T. 2000, ApJ, 120, 2331
- Toft, S., Pedersen, K., Ebeling, H. & Hjorth, J. 2003, MNRAS, 341, L55
- Totani, T., Yoshii, Y., Maihara, T., Iwamuro, F., & Motohara, K. 2001, ApJ, 559, 592
- Väisänen, P. & Johansson, P.H. 2004a, A&A, 421, 821
- Väisänen, P. & Johansson, P.H. 2004b, A&A, 422, 453
- Wold, M., Armus, L., Neugebauer, G., Jarrett, T.H., & Lehnert, M.D. 2003, AJ, 126, 1776
- Yan, L., & Thompson, D. 2003, ApJ, 586, 765
- Yan, L., Thompson, D., & Soifer, B.T. 2004a, AJ, 127, 1274
- Yan, L., et al. 2004b, ApJS, 154, 75

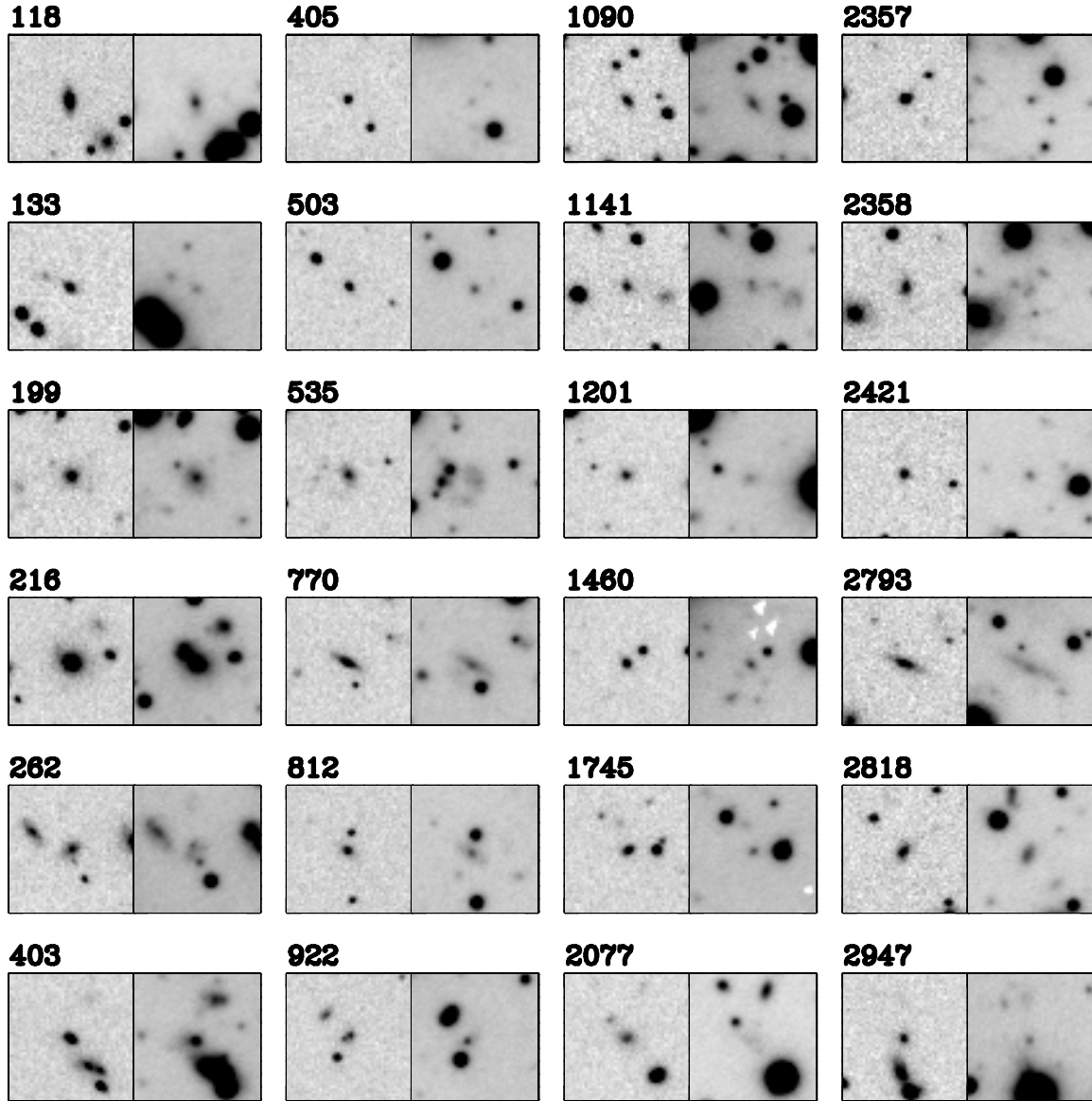


FIG. 7.— EROs with  $K_S < 19$  and  $R - K_S > 5.3$ . Shown are  $K_S$  (left) and  $R$  (right) image pairs. Each image is  $10''$  on the side and the ERO is at its center. Seeing is  $0.4''$  and  $0.6''$  in the  $K_S$  and  $R$  images, respectively.

TABLE 1. ERO CATALOG

ID	R.A.(2000) <sup>a</sup>	Decl.(2000) <sup>a</sup>	$K_S$	$R-K_S$	Class <sup>b</sup>
100	19:24:04.153	-21:00:16.291	19.80±0.14	5.49±0.18	R
107	19:24:06.006	-21:00:13.966	20.89±0.24	7.75±1.14	R
118	19:24:06.639	-21:00:14.985	17.52±0.04	6.13±0.06	R
133	19:24:16.166	-21:00:13.325	18.49±0.07	6.48±0.10	R
178	19:24:10.310	-21:00:08.392	19.72±0.14	6.56±0.30	R
199	19:24:10.014	-21:00:07.581	17.86±0.05	5.39±0.08	R
216	19:24:16.590	-21:00:01.166	16.50±0.03	5.39±0.04	R
262	19:24:16.961	-21:00:01.876	18.29±0.07	5.70±0.11	R
283	19:24:09.002	-20:59:56.030	20.76±0.23	6.35±0.44	R
344	19:24:13.313	-20:59:51.544	20.73±0.21	6.88±0.47	U
403	19:24:15.137	-20:59:45.207	17.81±0.05	5.37±0.07	R
405	19:24:22.275	-20:59:46.121	18.99±0.08	7.32±0.16	U
434	19:24:04.166	-20:59:44.781	19.25±0.11	6.55±0.21	R
500	19:24:20.954	-20:59:37.389	20.49±0.20	5.33±0.24	U
503	19:24:16.621	-20:59:38.249	18.97±0.09	5.83±0.10	R
535	19:24:17.240	-20:59:33.670	18.47±0.07	5.79±0.11	R
553	19:24:05.754	-20:59:32.043	20.22±0.16	6.02±0.20	U
576	19:24:21.612	-20:59:29.631	20.77±0.21	6.72±0.44	U
609	19:24:21.470	-20:59:28.234	19.79±0.13	5.91±0.19	U
612	19:24:19.627	-20:59:27.080	19.20±0.09	5.36±0.10	U
616	19:24:17.366	-20:59:27.731	20.33±0.23	5.54±0.32	R
642	19:24:21.559	-20:59:24.399	20.35±0.17	6.85±0.34	U
674	19:24:17.801	-20:59:20.601	20.83±0.22	5.86±0.29	U
703	19:24:04.883	-20:59:19.663	20.27±0.17	5.59±0.25	R
727	19:24:19.087	-20:59:17.119	19.38±0.10	5.94±0.13	R
733	19:24:21.244	-20:59:15.076	20.50±0.19	6.54±0.35	U
734	19:24:06.165	-20:59:15.414	20.20±0.16	6.62±0.29	U
770	19:24:17.346	-20:59:11.068	18.02±0.06	5.84±0.08	R
812	19:24:09.283	-20:59:10.339	18.74±0.08	5.46±0.10	R
922	19:24:13.296	-20:58:59.767	18.91±0.09	5.63±0.12	R
925	19:24:17.886	-20:58:57.131	20.23±0.16	5.71±0.25	R
958	19:24:15.883	-20:58:55.029	19.13±0.10	6.10±0.15	R
1000	19:24:21.840	-20:58:48.904	20.53±0.18	5.43±0.21	U
1024	19:24:03.510	-20:58:47.091	19.73±0.13	6.02±0.16	U
1041	19:24:15.019	-20:58:44.183	20.55±0.21	5.39±0.26	R
1090	19:24:15.735	-20:57:12.278	18.80±0.08	5.51±0.10	R
1117	19:24:20.440	-20:57:14.743	20.12±0.16	7.50±0.60	U
1141	19:24:15.567	-20:57:16.962	18.87±0.09	5.58±0.11	R
1194	19:24:20.899	-20:57:23.016	19.95±0.14	6.64±0.25	R
1201	19:24:10.625	-20:57:24.242	18.96±0.09	6.05±0.12	R
1205	19:24:22.583	-20:57:24.495	19.86±0.14	6.77±0.25	U
1210	19:24:13.322	-20:57:25.375	20.14±0.17	5.80±0.27	R
1230	19:24:10.732	-20:57:28.299	20.76±0.22	5.57±0.27	U
1260	19:24:14.692	-20:57:31.466	20.41±0.17	6.86±0.42	R
1272	19:24:17.349	-20:57:33.207	19.58±0.11	5.53±0.13	U
1375	19:24:17.493	-20:57:43.703	19.92±0.13	7.11±0.28	U
1448	19:24:11.548	-20:57:51.816	20.92±0.22	6.28±0.36	U
1460	19:24:09.808	-20:57:53.466	18.80±0.08	5.68±0.10	R
1569	19:24:15.035	-20:58:02.903	20.11±0.19	5.87±0.31	R
1646	19:24:14.623	-20:58:09.749	20.77±0.24	6.58±0.60	U
1734	19:24:20.134	-20:58:19.264	20.33±0.20	5.88±0.35	R
1745	19:24:15.717	-20:58:19.985	18.64±0.07	6.06±0.10	R
1789	19:24:15.406	-20:58:25.431	20.83±0.21	9.12±3.57	U
1790	19:24:16.733	-20:58:25.371	20.21±0.15	5.75±0.19	U
1800	19:24:15.027	-20:58:26.166	20.21±0.16	6.65±0.29	U
1812	19:24:11.958	-20:58:28.127	19.84±0.15	5.70±0.23	R
1857	19:24:08.225	-20:58:31.597	19.82±0.13	5.57±0.15	U
1885	19:24:07.314	-20:58:34.855	20.70±0.21	6.17±0.35	U
1890	19:24:20.748	-20:58:35.387	19.11±0.09	5.44±0.10	U
1903	19:24:03.393	-20:58:37.094	19.26±0.10	5.93±0.14	R
1909	19:24:05.028	-20:58:37.544	20.06±0.16	5.95±0.25	R
1910	19:24:14.965	-20:58:37.180	19.91±0.13	5.56±0.15	U
1954	19:24:21.713	-20:58:41.015	19.59±0.11	6.64±0.19	U
1968	19:24:06.793	-20:58:41.701	20.30±0.16	6.01±0.24	R
1975	19:24:17.631	-20:58:42.206	20.05±0.15	5.51±0.20	U
1997	19:24:06.774	-20:58:44.191	19.91±0.13	6.55±0.19	U
2074	19:24:11.190	-20:55:34.000	20.46±0.19	6.00±0.30	U
2077	19:24:04.688	-20:55:35.005	18.34±0.07	6.13±0.13	R
2079	19:24:06.088	-20:55:33.537	19.98±0.14	5.45±0.17	U
2094	19:24:07.354	-20:55:35.030	20.25±0.18	5.43±0.22	R
2147	19:24:20.278	-20:55:39.935	20.39±0.18	6.91±0.40	R
2157	19:24:07.113	-20:55:42.978	19.96±0.14	5.78±0.17	U
2158	19:24:11.087	-20:55:40.270	20.19±0.18	5.87±0.26	U
2169	19:24:16.784	-20:55:44.154	19.90±0.15	6.74±0.38	R
2205	19:24:06.131	-20:55:46.907	19.22±0.10	6.23±0.15	R
2220	19:24:18.437	-20:55:49.874	19.82±0.13	6.40±0.24	R

TABLE 1. ERO CATALOG— *Continued*

ID	R.A.(2000) <sup>a</sup>	Decl.(2000) <sup>a</sup>	$K_S$	$R-K_S$	Class <sup>b</sup>
2222	19:24:18.497	-20:55:48.347	19.02±0.10	6.65±0.25	R
2242	19:24:16.721	-20:55:49.549	20.19±0.16	6.03±0.22	U
2254	19:24:22.603	-20:55:44.150	20.21±0.16	5.83±0.21	R
2273	19:24:20.242	-20:55:52.398	19.12±0.09	5.32±0.11	U
2319	19:24:22.274	-20:55:55.092	19.28±0.10	5.62±0.11	U
2357	19:24:19.035	-20:56:00.043	17.73±0.05	7.03±0.06	U
2358	19:24:19.395	-20:55:59.749	18.27±0.06	6.05±0.10	R
2410	19:24:08.136	-20:56:07.100	20.21±0.16	6.15±0.22	R
2421	19:24:18.527	-20:56:07.702	18.82±0.08	6.10±0.10	R
2475	19:24:09.125	-20:56:11.069	20.79±0.21	5.94±0.27	U
2482	19:24:19.322	-20:56:15.024	19.29±0.10	6.63±0.16	R
2509	19:24:19.068	-20:56:15.785	19.22±0.10	5.82±0.12	U
2588	19:24:21.415	-20:56:14.121	20.30±0.17	6.05±0.23	R
2628	19:24:11.911	-20:56:27.323	20.79±0.21	7.99±1.27	U
2659	19:24:05.032	-20:56:32.229	19.42±0.11	8.14±0.84	R
2742	19:24:10.715	-20:56:40.164	20.30±0.16	5.35±0.19	R
2756	19:24:20.964	-20:56:40.937	20.11±0.18	5.82±0.30	R
2791	19:24:19.299	-20:56:43.208	19.77±0.13	6.59±0.24	R
2793	19:24:21.152	-20:56:44.473	17.85±0.05	6.29±0.09	R
2818	19:24:20.345	-20:56:45.692	18.40±0.07	5.52±0.09	R
2899	19:24:04.041	-20:56:54.393	20.99±0.27	6.52±0.59	U
2947	19:24:14.613	-20:56:58.961	18.56±0.07	5.82±0.11	U
2985	19:24:15.132	-20:57:02.388	19.27±0.10	6.03±0.12	U
3012	19:24:15.093	-20:57:06.766	19.77±0.13	5.37±0.15	R
3033	19:24:22.498	-20:57:07.613	19.35±0.11	5.67±0.14	R

TABLE 2. MORPHOLOGICAL PROPERTIES OF  $K_S < 19$  EROS

ID	$K_S$	$R-K_S$	morphology <sup>a</sup>
118	17.52	6.13	BD
133	18.49	6.48	BD
199	17.86	5.39	BD
216	16.50	5.39	?
262	18.29	5.70	I
403	17.81	5.37	I
405	18.99	7.32	U
503	18.97	5.83	?
535	18.47	5.79	DI
770	18.02	5.84	BD
812	18.74	5.46	BD
922	18.91	5.63	I
1090	18.80	5.51	BD
1141	18.87	5.58	BD
1201	18.96	6.05	?
1460	18.80	5.68	?
1745	18.64	6.06	?
2077	18.34	6.13	BD
2357	17.73	7.03	U
2358	18.27	6.05	I
2421	18.82	6.10	?
2793	17.85	6.29	BD
2818	18.40	5.52	BD
2947	18.56	5.82	U

<sup>a</sup> Positions taken from the World Coordinate System of the  $R$ -band image.<sup>b</sup> Star-galaxy separation: R — Resolved, U — Uncertain<sup>a</sup> D: disk, B: bulge, I: signs of interaction or close companion, U: morphologically uncertain (possible star — see § 3.2), ?: galaxy but otherwise morphologically unclassified (i.e., not a star)